PAPER

Ni₃FeN functionalized carbon nanofibers boosting polysulfide conversion for Li–S chemistry†

Lufu Xu, Huani Li, Genfu Zhao, Yongjiang Sun, Han Wang and Hong Guo [ID] *

Limiting the shuttle effect of polysulfides is an important means to realizing high energy density lithium–sulfur batteries (Li–S). In this study, an efficient electrocatalyst (CNFs@Ni₃FeN) is synthesized by anchoring Ni₃FeN in the carbon nanofibers (CNFs). The CNFs@Ni₃FeN shows electrocatalytic activity and enhances the conversion of polysulfides. After assembling a battery, a high initial capacity (1452 mA h g⁻¹) and favorable long-time cycling stability (100 cycles) with a capacity retention rate of 83% are obtained by the electrocatalysis of Ni₃FeN. Compared with unmodified CNFs, the cycling stability of CNFs@Ni₃FeN can be greatly improved. The catalytic mechanism is further deduced by X-ray photoelectron spectroscopy (XPS). Our work will inspire the rational design of CNFs@support hybrids for various electrocatalysis applications.

Introduction

In the past decades, the demand for high energy density energy storage devices has promoted the development of many energy storage systems, such as lithium-ion battery technology, sodium-ion battery technology and so on. The most representative energy storage system is the lithium-ion battery.[1–3] Lithium-ion batteries are also widely used in our society because of their relatively high energy density.[4] However, lithium-ion batteries have some shortcomings, such as low abundance of lithium resources, uneven distribution and low energy density, so their further development is limited.[5] Previous research shows that lithium–sulfur batteries (Li–S battery) have an energy density as high as 2600 W h kg⁻¹ and a theoretical specific capacity of 1675 mA h g⁻¹. So, Li–S battery is promising to become the next generation energy storage system after lithium-ion battery.[6]

As the positive active material, sulfur (S₈) participates in the charge compensation in the process of charge and discharge in Li–S battery. The discharge process of Li–S battery can be divided into three stages.[6,7] In the first stage, sulfur (S₈) is reduced to form S₄²⁻ by step-by-step sequence reduction of soluble polysulfide ions, and the reaction speed is fast (voltage platform ∼2.3 V vs. Li/Li⁺). It is worth noting that various intermediate polysulfides (Li₂Sₓ, x = 8–4) will be formed in this process. These polysulfides are highly dissolved in organic electrolytes, resulting in irreversible capacity loss. For example, high-order polysulfides are conversed into low-order polysulfides (Li₂S or Li₂S₂) and deposited the surface of lithium anode. This process will reduce the utility of active material sulfur and the coulombic efficiency in charge–discharge process. In the second stage, the soluble lithium polysulfide Li₂S₄ is reduced to insoluble Li₂S₂, and the voltage platform is 2 V vs. Li/Li⁺. This process is controlled by the solid phase nucleation reaction, so the reaction rate is slow. In the third stage, solid phase Li₂S₂ is reduced to solid phase Li₂S, which is controlled by solid phase diffusion of Li ions, so the reaction rate is slow.[8] The capacity contribution of these three stages is 25%, 25% and 50%, respectively.[9] Compared with the discharge process, the charge process is relatively simple. In the cyclic voltammetry (CV) of sulfur or polysulfide electrodes, typically there is only one anodic peak.[10] Although the lithium–sulfur battery has high specific capacity and rich mineral resources, its development still faces many challenges, such as low conductivity of positive active material sulfur (S₈),[11] shuttle effect of polysulfides, slow reaction kinetics and large volume change in charge–discharge process.

At present, there are mainly the following strategies to overcome the problem of polysulfide shuttle effect: (1) physically limiting the active material sulfur to porous conductive materials;[12–14] (2) chemical adsorption the polysulfides with defective carbon,[15–17] transition metal oxides,[18–20] MXene,[21,22] transition metal nitride,[23] and so on; (3) microstructure design with graphene[24–27] or carbon materials[28–30] to prepare free-standing electrodes or three-dimensional electrodes;[30–32] and (4) introducing a conductive intermediate layer between separator and cathode to alleviate the shuttle effect of the polysulfides.[33–38] Among them, transition metal nitride has attracted considerable attention in Li–S batteries because the catalysts efficiently accelerate the conversion of the lithium polysulfides and actually inhibit polysulfide shuttling. Especially for the

School of Materials and Energy, Yunnan University, Kunming 650091, China. E-mail: guohong@ynu.edu.cn

Ni_3FeN material with highly exposed active sites and high electrical conductivity has been developed to enhance the electrocatalytic activity in oxygen evolution reaction (OER).[39] Considering that sulfur and oxygen have similar electrochemical redox mechanisms, Ni_3FeN is also used as a sulfur promoter to promote the conversion of polysulfides.

In this work, we use $CNFs@Ni_3FeN$ composites to alleviate the shuttle effect of polysulfides in the charge–discharge process, and enhance the coulomb efficiency and cycle stability of Li–S battery in the charge–discharge process. The Ni_3FeN in the material can implement the adsorption of soluble polysulfides produced in the process of charge and discharge and alleviate the shuttle effect in the process of cycle. At the same time, it can also catalyze the conversion of polysulfides to S_2^{2-} and the oxidation of Li_2S during charging, so as to reduce the existence time of soluble polysulfides and alleviate the shuttle effect of polysulfides.[40–42] The carbon nanofibers in the materials provide a three-dimensional supporting conductive skeleton for the cathode materials. Therefore, through the synergistic effect of Ni_3FeN and CNFs, high-performance Li–S battery can be achieved.

Materials

All the chemical materials and characterized apparatus are described in the ESI.†

Results and discussions

tThe crystal structural characteristics of CNFs, Ni_3FeN and $CNFs@Ni_3FeN$ were detected by X-ray diffraction (XRD) analysis, illustrated in Fig. 1a. From the diagram, we can observe that the peak position of the Ni_3FeN material coincides well with that of the Ni_3FeN standard card (PDF: 00-050-1434), indicating that the ternary phase Ni_3FeN has been synthesized successfully.[39] The characteristic peak of Ni_3FeN is strong and sharp, implying that the synthesized Ni_3FeN has high crystallinity. Comparing the XRD spectra of CNFs, Ni_3FeN and $CNFs@Ni_3FeN$, we find that $CNFs@Ni_3FeN$ not only has the characteristic peak of Ni_3FeN crystal, but also has the same peak as CNFs, certifying that Ni_3FeN and CNFs were successfully compounded by electrospinning. Fig. 1b shows the Raman spectra of CNFs, Ni_3FeN and $CNFs@Ni_3FeN$. It can be observed that there are two typical G-band peaks in CNFs and $CNFs@Ni_3FeN$ materials, which are located at 1354.17 cm^{-1} and 1587.34 cm^{-1} respectively. The peak-to-intensity ratio of D-band and G-band is 1.05, proving that the structure of CNFs is mainly short-range ordered graphite structure.[43] The low graphitization degree of the carbon in $CNFs@Ni_3FeN$ can promote the migration of Li^+ during the cycle.[42] In addition, we can find that there is a Raman peak of Ni_3FeN (546.988 cm^{-1}) in $CNFs@Ni_3FeN$ materials, which further proves that $CNFs@Ni_3FeN$ is successfully synthesized. As depicted in Fig. 1c–e, the scanning electron microscopy (SEM) and transmission electron microscopy (TEM) images show that Ni_3FeN nanoparticles are well dispersed on the carbon nanofiber. From the SEM images of CNFs and $CNFs@Ni_3FeN$, it can be observed that the average diameter of CNFs and $CNFs@Ni_3FeN$ is about

300 nm. According to TEM figure, Ni_3FeN nanoparticles are crystallized on the inner of carbon nanofiber. The d-spacings of 0.215 nm correspond to the (111) planes of Ni_3FeN.[39] This further verifies that Ni_3FeN is well compounded with carbon nanofibers.

For the purpose of exploring the load of sulfur in the host materials, the thermogravimetric analysis (TGA) of $CNFs@Ni_3FeN@S$ was collected and shown in Fig. 1f. It can be seen that the mass loss of $CNFs@Ni_3FeN@S$ sample is 77.03 wt%, but there is no obvious mass change of $CNFs@Ni_3FeN$ sample. The result reveals that the load of sulfur is about 77.03 wt%. In order to further analyze the total surface area and micropore volume of the CNFs and $CNFs@Ni_3FeN$, the nitrogen adsorption–desorption isotherms were carried out. The type of curve in Fig. S1a† is type IV, which manifests that there are abundant mesoporous structures. From the analysis, the total surface area and micropore volume of the CNFs are $228.521 \text{ m}^2 \text{ g}^{-1}$, $0.1017 \text{ cm}^3 \text{ g}^{-1}$, respectively and the $CNFs@Ni_3FeN$ are $107.265 \text{ m}^2 \text{ g}^{-1}$, $0.04857 \text{ cm}^3 \text{ g}^{-1}$, respectively. As exhibited in the Fig. S1b,† the pore size distribution of $CNFs@Ni_3FeN$ is between 2 and 5 nm, while that of CNFs is about 15 nm. It turns out that both materials are porous structure. The porous structure is conducive to electrolyte infiltration into the material and the transport of lithium ion in the electrode material.[44] Moreover, the relatively small specific surface area and pore size in $CNFs@Ni_3FeN$ can inhibit the bulky volumetric corrosion of the $CNFs@Ni_3FeN@S$ cathode occurring in the conversion reaction that might enhance the energy storage performances of $CNFs@Ni_3FeN$.[45]

The valence states of elements in $CNFs@Ni_3FeN$ and CNFs were determined by X-ray photoelectron spectroscopy (XPS), shown in Fig. 2a–d. From Fig. 2a, there are obvious peaks of Fe, Ni, N and S in Ni_3FeN and $CNFs@Ni_3FeN/Li_2S_4$. The C and O elements with strong peaks in the picture may come from the raw materials in the process of Ni_3FeN preparation. Fig. 2b and c are the XPS spectrum of Ni 2p and Fe 2p, respectively. The result reveals that the element of Ni is in the state of Ni^{2+} and Ni^0, and the element of Fe is in the state of Fe^{3+} and Fe^0. The existence of Ni^{2+} and Fe^{3+} may be related to the existence of some inevitable surface oxide layer in Ni_3FeN.[46–48] Compared with $CNFs@Ni_3FeN$, the Ni $2p_{3/2}$ spectrum of $CNFs@Ni_3FeN/Li_2S_4$ shifts to the direction of low binding energy (0.3 eV). These changes indicate that there is a charge transfer between Ni and S in Li_2S_4, and the electrons on S atoms are transferred to Ni atoms.[49] In the Fe $2p_{3/2}$ spectrum of Fig. 2c, we can see that all the peaks in the Fe $2p_{3/2}$ spectrum (712.6 eV) of $CNFs@Ni_3FeN$ after polysulfide adsorption shift 0.4 eV to the direction of low binding energy, revealing that electrons are transferred from S atoms in Li_2S_4 to Fe atoms.[49] Fig. 2d is the N 1s spectrum. After the reaction with polysulfides, the N 1s spectrum of $CNFs@Ni_3FeN/Li_2S_4$ shifts significantly to higher binding energy than that of $CNFs@Ni_3FeN$ (0.6 eV). This phenomenon may result from the transfer of electrons from N atom to metal atoms. The XPS spectra of Ni $2p_{3/2}$, Fe $2p_{3/2}$ and N 1s show that Ni_3FeN has a strong adsorption effect on polysulfides.

In addition, static visible light adsorption experiments were implemented to visualize the anchoring ability between Ni_3FeN and polysulfides. CNFs and $CNFs@Ni_3FeN$ with the same specific surface area were immersed into the Li_2S_4
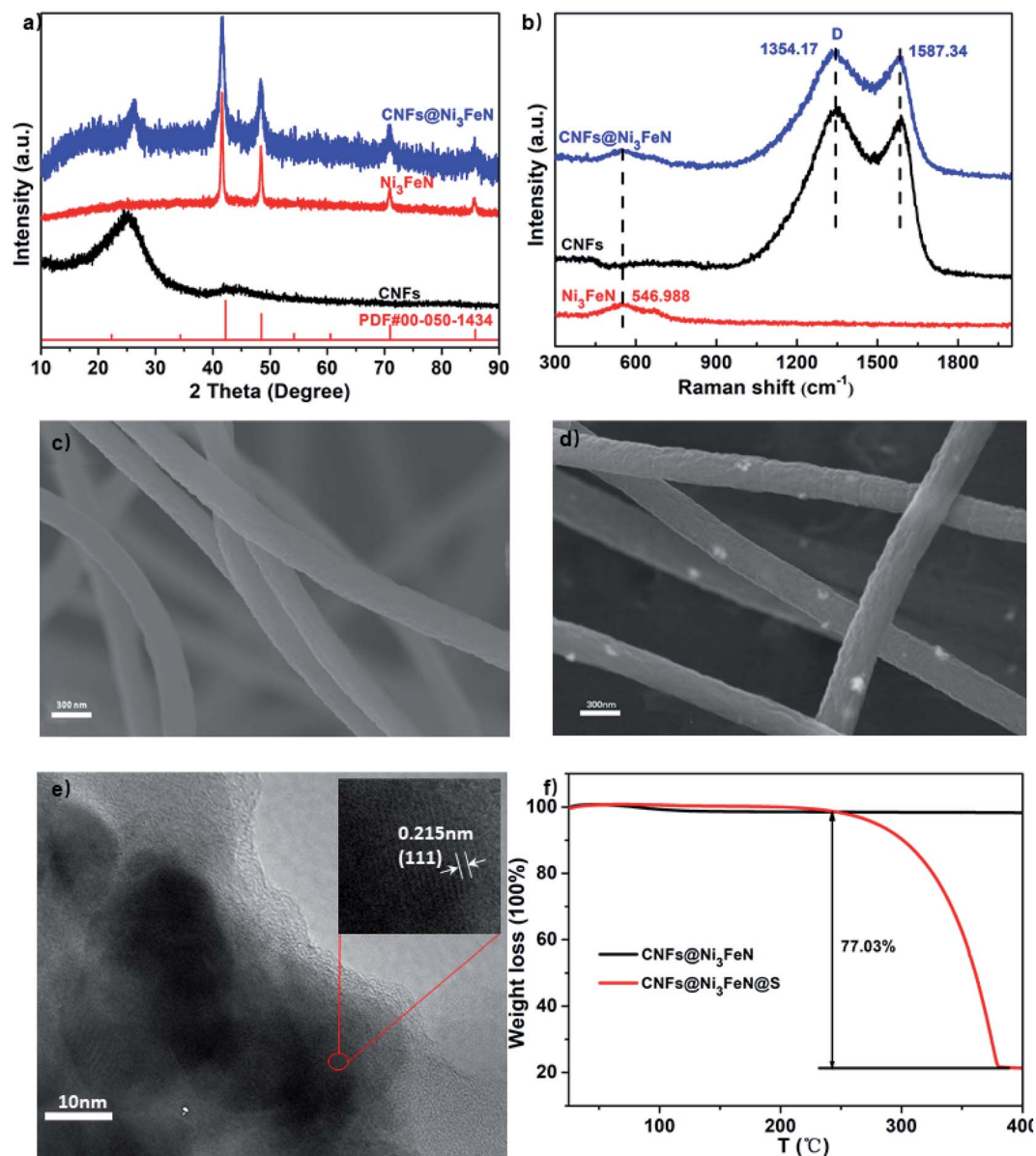
Fig. 1 (a) XRD patterns of Ni₃FeN, CNFs and CNFs@Ni₃FeN. (b) Raman spectra of Ni₃FeN, CNFs and CNFs@Ni₃FeN. SEM images of (c) CNFs and (d) CNFs@Ni₃FeN. (e) TEM images of CNFs@ Ni₃FeN. (f) TGA curves of CNFs@Ni₃FeN and CNFs @Ni₃FeN@S.

electrolyte of 1.5 mL. After that, they were placed in a glove box for 3 h. We can observe in Fig. 2e that the color of Li_2S_4 solution immersed with CNFs is still yellow and does not fade, while the color of Li_2S_4 solution immersed with CNFs@Ni₃FeN has completely faded. The results show that Ni₃FeN has a strong adsorption effect on polysulfides. For further studying the interaction between CNFs@Ni₃FeN@S and Li_2S_4, XPS studies on Li_2S_4 and CNFs@Ni₃FeN@S–Li_2S_4 were carried out. As shown in Fig. 2f, the peaks at 161.8 eV and 163.6 eV in the S 2p spectrum correspond to terminal (S_T^{-1}) and bridged (S_B^0) sulfur atoms. However, when CNFs@Ni₃FeN@S was added to the Li_2S_4 solution in Fig. 2g, S_T^{-1} (162.8 eV) and S_B^0 (163.9 eV) in the S 2p spectrum shifted to varying degrees, and they moved 1.0 and 0.3 eV, respectively. At the same time, there are

new peaks at 162.5/161.9 eV and 161.1 eV, which belongs to Ni–S bond and Fe–S bond, respectively. The appearance of these two bonds indicate that CNFs@Ni₃FeN@S has a strong chemisorption to Li_2S_4.[50,51] In addition, we can see that there is a sulfate peak at 165–168 eV and a thiosulfate peak at 168 eV, which may be related to the disproportionation of intermediate Li_2S_x to produce higher and lower oxidized substances.[52–55] Moreover, we can find that the peaks of these two places are weakened to some extent after the addition of CNFs@Ni₃FeN, which disclose that CNFs@Ni₃FeN can better catalyze the transformation of Li_2S_4 to low-valent reduced state. The above analyses imply that the electrocatalyst was successfully prepared and shown good adsorption and catalytic capacity for polysulfide.
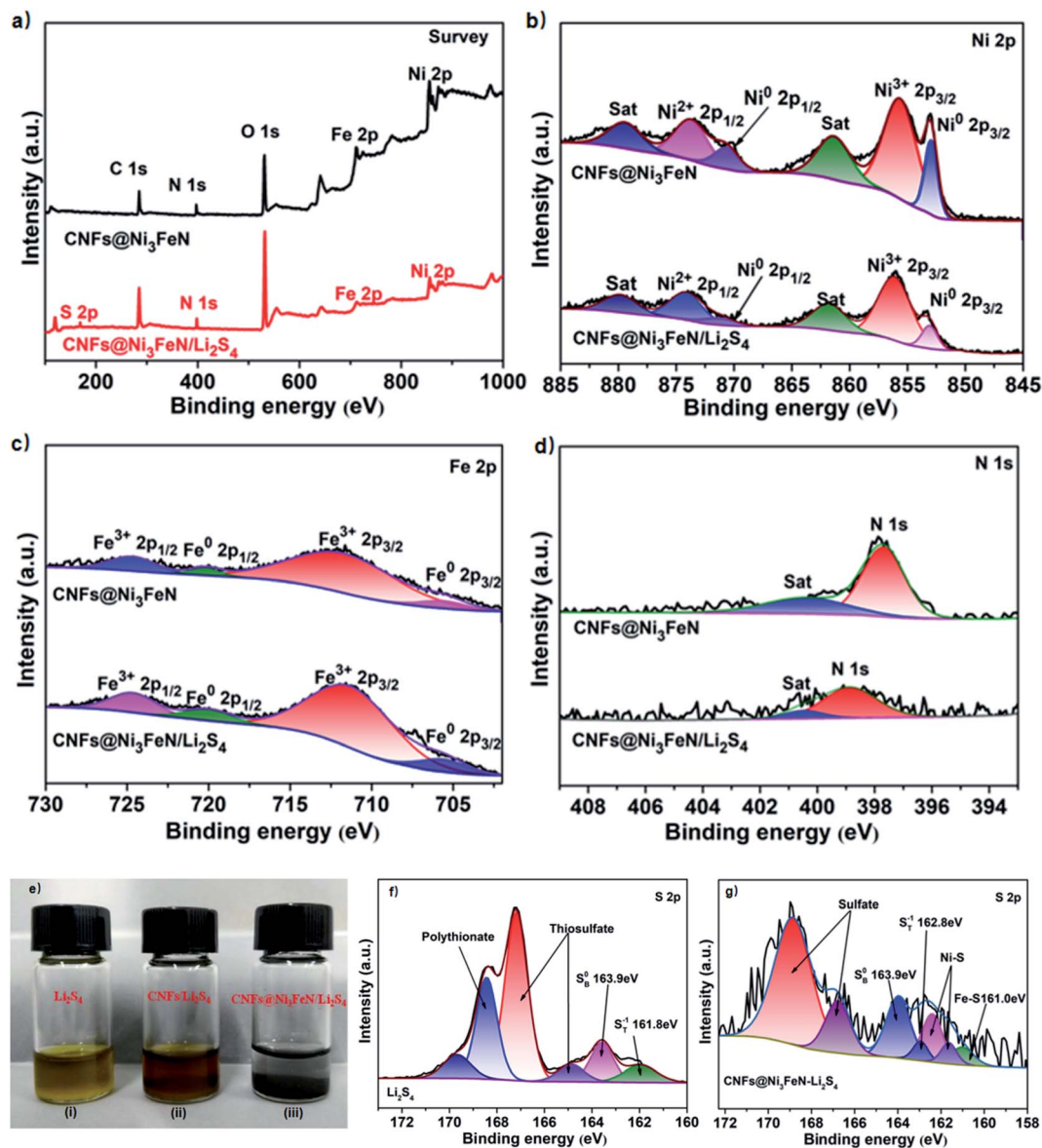
Fig. 2 (a–d) XPS spectra of the CNFs and CNFs@Ni$_3$FeN. (a) Full spectrum, (b) Ni 2p, (c) Fe 2p, (d) N 1s. (e) Photographs of a Li$_2$S$_4$ solution (i) Li$_2$S$_4$ solution added with CNFs (ii) and Li$_2$S$_4$ solution added with CNFs@Ni$_3$FeN (iii). (f) XPS S 2p spectra of Li$_2$S$_4$ and (g) XPS S 2p spectra of CNFs@Ni$_3$FeN/Li$_2$S$_4$.

The electrochemical storage properties of CNFs@S and CNFs@Ni$_3$FeN@S electrodes were studied by using coin cell and lithium sheet as counter electrode. The CV curves of CNFs@S and CNFs@Ni$_3$FeN@S are shown in Fig. 3a. The typical cathode peaks appear at 2.0 V and 2.3 V, which is attributed to the formation and conversion of long-chain polysulfides to Li$_2$S. The continuous anodizing peaks at 2.3–2.5 V are the transition from Li$_2$S/Li$_2$S$_2$ to polysulfide. CNFs@Ni$_3$-FeN@S shows the sharpest and highest anodic peak, which implies that the conversion process from Li$_2$S to polysulfides is more thorough. At the same time, the CNFs@Ni$_3$FeN also shows better catalytic behavior to promote the transformation of polysulfides. Fig. 3b presents the CV curves of the five circles of CNFs@Ni$_3$FeN@S. It can be seen that the coincidence of

cathode peak and anode peak is very good. The result demonstrates that the Li–S battery assembled with CNFs@Ni$_3$FeN@S as positive electrode has excellent charge–discharge cycle stability and the reversible reaction is more favorable from S$_8$ to Li$_2$S/Li$_2$S$_2$.[56]

To further quantitatively analyze the catalytic kinetic rate of polysulfide conversion process, the Tafel slopes of the first reduction and oxidation processes were obtained in Fig. 3c and d, respectively. For the first reduction peak, the Tafel slopes of CNFs@S and CNFs@Ni$_3$FeN@S are 41.0 and 57.6 mV dec^{-1}, respectively. For the first oxidation peak, the Tafel slopes of CNFs@S and CNFs@Ni$_3$FeN@S are 76.0 and 62.9 mV dec^{-1}, respectively. The Tafel slope of lithium–sulfur battery assembled with *in situ* synthesized CNFs@Ni$_3$FeN@S as positive
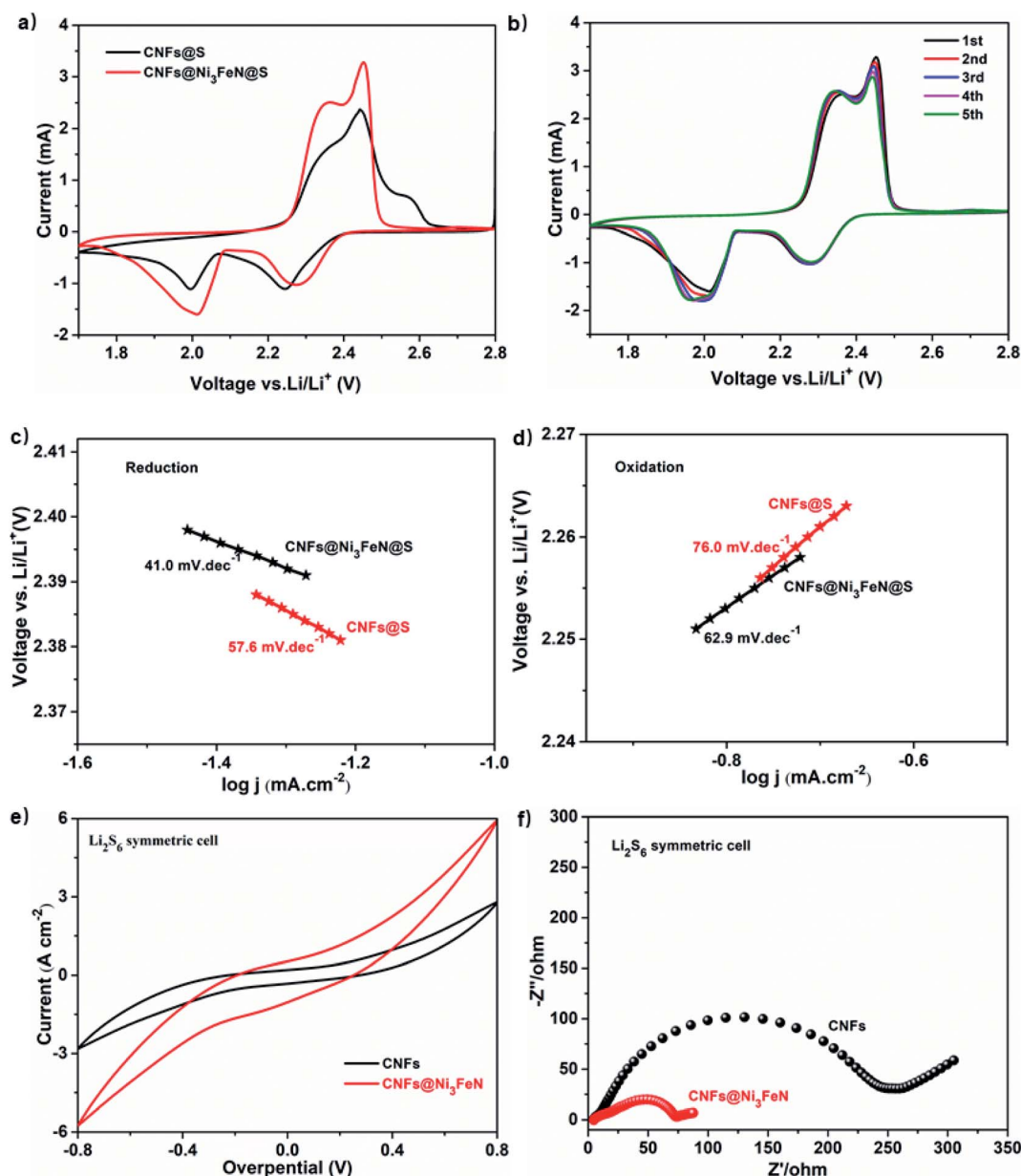
Fig. 3 CV curves at the scan rate of 0.1 mV s^{-1} in a potential window from 1.7 to 2.8 V of (a) the CNFs@Ni$_3$FeN and CNFs@Ni$_3$FeN@S electrodes and (b) the first five cycles of CNFs@Ni$_3$FeN@S. Tafel plots of the (c) first reduction peak and (d) the oxidation peak. (e) CV curves of symmetric cells and (f) EIS Nyquist plots obtained from CNFs@Ni$_3$FeN and CNFs@Ni$_3$FeN@S electrodes.

electrode is relatively small, which clearly confirms that the reaction between liquid polysulfide and solid sulfur is easier, and the electrocatalyst Ni$_3$FeN promotes the conversion of polysulfide.[57] Symmetrical cells were assembled for CV and Electrochemical impedance spectroscopy (EIS) tests to further explore the catalytic performance of CNFs and CNFs@Ni$_3$FeN. As showcase in Fig. 3e, when the voltage bias is 0.8 V, the redox current response of CNFs@Ni$_3$FeN is nearly twice that of CNFs, implying that Ni$_3$FeN can enhance the conversion efficiency and electrochemical reversibility of polysulfides to Li$_2$S.[58] The EIS measurements of CNFs and CNFs@Ni$_3$FeN are analyzed in Fig. 3f. It can be seen from the Nyquist diagram that the EIS of CNFs and CNFs@Ni$_3$FeN are composed of high frequency

semicircle, intermediate frequency semicircle and an inclined low frequency line. The high frequency semicircle is related to the charge transfer resistance (R_{ct}), the intermediate frequency semicircle is related to the establishment of the solid electrolyte interface (SEI) film resistance (R_s) produced during the irreversible aggregation of insoluble low-order polysulfide, and the inclined line is related to the Warburg impedance (W_e) of Li$^+$ diffusion in the electrode.[59] Obviously, compared with the CNFs@S electrode, the CNFs@Ni$_3$FeN@S displays smaller the solid electrolyte interface (SEI) film resistance (R_s). The excellent interface impedance results suggest that due to the existence of Ni$_3$FeN, the amount of irreversible insoluble low-order polysulfide at the electrode interface is reduced, thereby resulting in

enhanced the transformation of insoluble low-order polysulfide to higher-order polysulfide and S$_8$. Above results consistently demonstrate the efficient adsorption and catalytic polysulfide conversion capability of CNFs@Ni$_3$FeN.

The galvanostatic charge–discharge curves of CNFs@S and CNFs@Ni$_3$FeN@S composites at 0.1C (1C = 1675 mA h g^{-1}) are witnessed in Fig. 4a. At ~2.3 V and ~2.1 V, the two typical high discharge platforms and low discharge platforms refer to the adsorption level and conversion level of polysulfides, respectively.[42] This is consistent with the analysis of the CV curve.

CNFs@Ni$_3$FeN@S composite nanostructure materials can provide high initial discharge capacity of 1406.5 mA h g^{-1}, which is much higher than that of CNFs@S (1156.9 mA h g^{-1}). The charge–discharge platform of CNFs@Ni$_3$FeN@S is longer, indicating that it has the ability to improve the utilization of active materials and promote the conversion between solid sulfide and long-chain polysulfides. In addition, to further confirm that CNFs@Ni$_3$FeN@S can better adsorb and catalyze polysulfides, we used CNFs@Ni$_3$FeN@S and CNFs@S as positive electrodes to test the charge–discharge cycle performance of
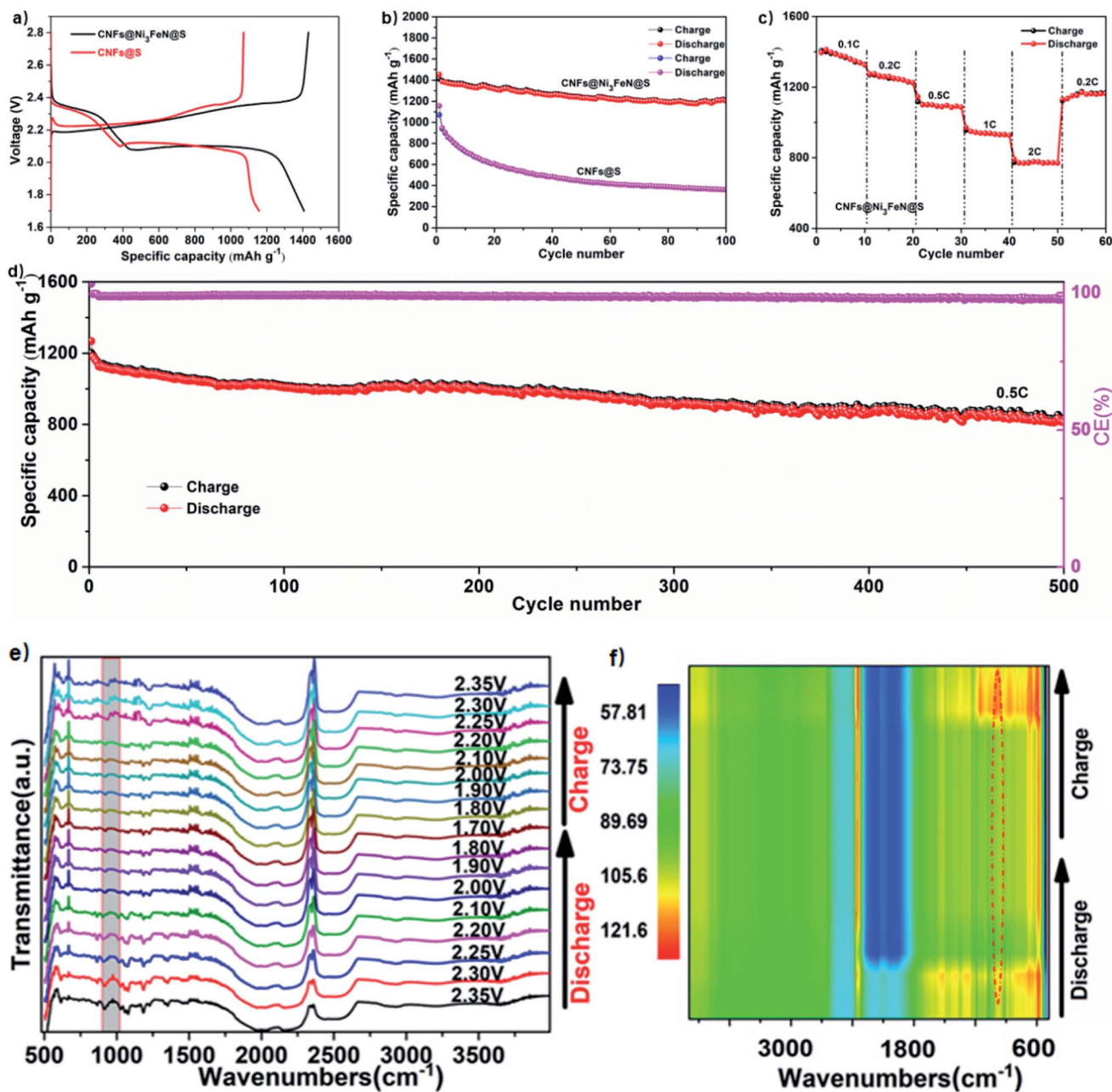

Fig. 4 (a) Reversible discharge/charge voltage profiles at 0.1C of CNFs@S and CNFs@Ni$_3$FeN@S electrodes. (b) Cycle performances at 0.1C of CNFs@S and CNFs@Ni$_3$FeN@S electrodes. (c) Rate performances of CNFs@Ni$_3$FeN@S electrodes at 0.1C, 0.2C, 0.5C, 1C and 2C rates. (d) Long-term cycling performances of CNFs@Ni$_3$FeN electrodes at 0.5C. (e) In situ FT-IR spectra of CNFs@Ni$_3$FeN@S cathode at different discharge and charge states. (f) Contour and response surface analysis corresponding to the discharge and charge processes.

the battery at 0.1C. As can be seen from Fig. 4b, the initial discharge specific capacities of CNFs@Ni$_3$FeN@S and CNFs@S are 1452.2 mA h g^{-1} and 1156.9 mA h g^{-1}, respectively. After 100 cycles, the discharge specific capacities of CNFs@Ni$_3$FeN@S and CNFs@S are 1203.7 mA h g^{-1} and 358.2 mA h g^{-1}, respectively. The results imply that the Ni$_3$FeN can effectively adsorb polysulfides and catalyze the conversion of polysulfides.

The rate performance of CNFs@Ni$_3$FeN@S cathode at various current rates from 0.1C to 2C was evaluated in the voltage range from 1.7 to 2.8 V. As depicted in Fig. 4c, the discharge capacities of CNFs@Ni$_3$FeN@S cathode exhibit 1372.4, 1261.9, 1097.1, 937.1, and 781.2 mA h g^{-1} at 0.1, 0.2, 0.5, 1, and 2C, respectively. Impressively, once the current rate switched back to 0.2C, the CNFs@Ni$_3$FeN@S cathode can harvest an excellent capacity of 1129.5 mA h g^{-1}, which is attributed to the robust and stable structure.[40] Long-cycle stability is very important for commercial applications of lithium batteries. For evaluate the long-term cycle behavior of CNFs@Ni$_3$FeN@S, batteries using CNFs@Ni$_3$FeN@S cathodes are cycled at 0.5C for 500 times in Fig. 4d. After 500 cycles, the discharge capacity descends from 1267 mA h g^{-1} to 812 mA h g^{-1}, and the coulombic efficiency remains above 99%. The result displays that the CNFs@Ni$_3$FeN@S cathode has excellent long cycle performance, which can be attributed to the catalysis and adsorption of Ni$_3$FeN.

Furthermore, in order to fully understand the mechanism of action, we assembled the Li–S half cells for *in situ* Fourier transform infrared (FT-IR) measurement. The cathode material was CNFs@Ni$_3$FeN@S, the anode was lithium plate, the positive current collector was carbon paper, and the separator was Celgard polypropylene (PP) membrane. The electrolyte was 1 M LiTFSI dissolved in DME/DOL ($V_{DME} : V_{DOL} = 1 : 1$) solution, in addition, 2% LiNO$_3$ was used as additive. The result is illustrated in Fig. 4e and f. It is worth noticing that the intensities of the Li–S peak located at 933 cm^{-1} decrease and nearly disappear at the end of discharging, followed by reappearance upon charging, signifying the excellent reversibility of electrochemical reactions and effective restriction of polysulfides within the CNFs@Ni$_3$FeN@S‖Li@Li cell.

Conclusions

In summary, we proved that Ni$_3$FeN can be used as a highly efficient cathode catalyst for Li–S cells. In this paper, CNFs@Ni$_3$FeN materials with special micro-nano composite structure were synthesized *in situ* by electrospinning. Electrochemical tests and other physical characterizations show that, compared with CNFs, CNFs@Ni$_3$FeN not only has strong chemisorption effect on polysulfide intermediates, but also can significantly accelerate the transformation of polysulfides and alleviate the shuttle effect of Li–S cells. Our work explores a new way for the design and development of cathode materials for high-performance Li–S batteries, as well as providing a more reasonable method for the commercialization of Li–S cells.

Conflicts of interest

The authors declare no competing financial interest.

Acknowledgements

References

1 G. Zhao, H. Li, Z. Gao, L. Xu, Z. Mei, S. Cai, T. Liu, X. Yang, H. Guo and X. Sun, *Adv. Funct. Mater.*, 2021, 2101019.

2 G. Zhao, L. Xu, J. Jiang, Z. Mei, Q. An, P. Lv, X. Yang, H. Guo and X. Sun, *Nano Energy*, 2022, **92**, 106756.

3 Q. An, H. Wang, G. Zhao, S. Wang, L. Xu, H. Wang, Y. Fu and H. Guo, *Energy Environ. Sci.*, 2022, DOI: 10.1002/eem2.12345.

4 G. Zhao, Y. Zhang, Z. Gao, H. Li, S. Liu, S. Cai, X. Yang, H. Guo and X. Sun, *ACS Energy Lett.*, 2020, **5**, 1022–1031.

5 W. Weng, G. Liu, L. Shen and X. Yao, *J. Power Sources*, 2021, **512**, 230485.

6 K. Kumaresan, Y. Mikhaylik and R. E. White, *J. Electrochem. Soc.*, 2008, **155**, A576.

7 H. Yamin and E. Peled, *J. Power Sources*, 1983, **9**, 281–287.

8 H. Xu, S. Guo, W. Li and P. Yu, *Sci. Rep.*, 2015, **5**, 1–12.

9 X. Zhou, T. Liu, G. Zhao, X. Yang and H. Guo, *Energy Storage Mater*, 2021, **40**, 139–149.

10 H. Yamin, J. Penciner, A. Gorenshtain, M. Elam and E. Peled, *J. Power Sources*, 1985, **14**, 129–134.

11 Y. Yang, G. Zheng and Y. Cui, *Chem. Soc. Rev.*, 2013, **42**, 3018–3032.

12 W. Zhou, Y. Yu, H. Chen, F. J. DiSalvo and H. D. Abruña, *J. Am. Chem. Soc.*, 2013, **135**, 16736–16743.

13 J. S. Lee, J. Jun, J. Jang and A. Manthiram, *Small*, 2017, **13**, 1602984.

14 S. K. Park, J. Lee, T. Hwang, B. Jang and Y. Piao, *ACS Appl. Mater. Interfaces*, 2017, **9**, 2430–2438.

15 X. Song, S. Wang, Y. Bao, G. Liu, W. Sun, L. Ding, H. Liu and H. Wang, *J. Mater. Chem. A*, 2017, **5**, 6832–6839.

16 Z. Liu, J. Li, J. Xiang, S. Cheng, H. Wu, N. Zhang, L. Yuan, W. Zhang, J. Xie and Y. Huang, *Phys. Chem. Chem. Phys.*, 2017, **19**, 2567–2573.

17 W. Zhou, B. Guo, H. Gao and J. B. Goodenough, *Adv. Energy Mater.*, 2016, **6**, 1502059.

18 H. Wang, C. Fan, Y. Zheng, X. Zhang, W. Li, S. Liu, H. Sun, J. Zhang, L. Sun and X. Wu, *Chem.–Eur. J.*, 2017, **23**, 9666–9673.

19 Q. Sun, K. Chen, Y. Liu, Y. Li and M. Wei, *Chem.–Eur. J.*, 2017, **23**, 16312–16318.

20 X. He, H. Hou, X. Yuan, L. Huang, J. Hu, B. Liu, J. Xu, J. Xie, J. Yang and S. Liang, *Sci. Rep.*, 2017, **7**, 1–9.

21 X. Liang, A. Garsuch and L. F. Nazar, *Angew. Chem.*, 2015, **127**, 3979–3983.

22 M. Xiang, H. Wu, H. Liu, J. Huang, Y. Zheng, L. Yang, P. Jing, Y. Zhang, S. Dou and H. Liu, *Adv. Funct. Mater.*, 2017, **27**, 1702573.

23 Z. Cui, C. Zu, W. Zhou, A. Manthiram and J. B. Goodenough, *Adv. Mater.*, 2016, **28**, 6926–6931.

24 X. Zhao, H. Wang, G. Zhai and G. Wang, *Chem.–Eur. J.*, 2017, **23**, 7037–7045.

25 K. Zhang, K. Xie, K. Yuan, W. Lu, S. Hu, W. Wei, M. Bai and C. Shen, *J. Mater. Chem. A*, 2017, **5**, 7309–7315.

26 S. H. Chung and A. Manthiram, *Adv. Mater.*, 2018, **30**, 1705951.

27 M. R. Kaiser, Z. Ma, X. Wang, F. Han, T. Gao, X. Fan, J. Wang, H. K. Liu, S. Dou and C. Wang, *ACS Nano*, 2017, **11**, 9048–9056.

28 M. Li, R. Carter, A. Douglas, L. Oakes and C. L. Pint, *ACS Nano*, 2017, **11**, 4877–4884.

29 L. Sun, D. Wang, Y. Luo, K. Wang, W. Kong, Y. Wu, L. Zhang, K. Jiang, Q. Li and Y. Zhang, *ACS Nano*, 2016, **10**, 1300–1308.

30 A. Mentbayeva, A. Belgibayeva, N. Umirov, Y. Zhang, I. Taniguchi, I. Kurmanbayeva and Z. Bakenov, *Electrochim. Acta*, 2016, **217**, 242–248.

31 F. Wu, E. Zhao, D. Gordon, Y. Xiao, C. Hu and G. Yushin, *Adv. Mater.*, 2016, **28**, 6365–6371.

32 B. Xu, H. Wang, Q. Zhu, N. Sun, B. Anasori, L. Hu, F. Wang, Y. Guan and Y. Gogotsi, *Energy Storage Mater*, 2018, **12**, 128–136.

33 J. Y. Hwang, H. M. Kim, S. K. Lee, J. H. Lee, A. Abouimrane, M. A. Khaleel, I. Belharouak, A. Manthiram and Y. K. Sun, *Adv. Energy Mater.*, 2016, **6**, 1501480.

34 H. Shao, W. Wang, H. Zhang, A. Wang, X. Chen and Y. Huang, *J. Power Sources*, 2018, **378**, 537–545.

35 H. Peng, J. Huang, X. Liu, X. Cheng, W. Xu, C. Zhao, F. Wei and Q. Zhang, *J. Am. Chem. Soc.*, 2017, **139**, 8458–8466.

36 A. Paolella, D. Laul, V. Timoshevskii, W. Zhu, S. Marras, G. Bertoni, A. S. Wahba, G. Girard, C. Gagnon and L. Rodrigue, *J. Phys. Chem. C*, 2018, **122**, 1014–1023.

37 S. Lim, R. Lilly Thankamony, T. Yim, H. Chu, Y. Kim, J. Mun and T. Kim, *ACS Appl. Mater. Interfaces*, 2015, **7**, 1401–1405.

38 M. Shaibani, A. Akbari, P. Sheath, C. D. Easton, P. C. Banerjee, K. Konstas, A. Fakhfouri, M. Barghamadi, M. M. Musameh and A. S. Best, *ACS Nano*, 2016, **10**, 7768–7779.

39 X. Jia, Y. Zhao, G. Chen, L. Shang, R. Shi, X. Kang, G. I. Waterhouse, L. Z. Wu, C. H. Tung and T. Zhang, *Adv. Energy Mater.*, 2016, **6**, 1502585.

40 M. Wang, L. Fan, X. Sun, B. Guan, B. Jiang, X. Wu, D. Tian, K. Sun, Y. Qiu and X. Yin, *ACS Energy Lett.*, 2020, **5**, 3041–3050.

41 L. Wang, H. Wang, S. Zhang, N. Ren, Y. Wu, L. Wu, X. Zhou, Y. Yao, X. Wu and Y. Yu, *ACS Nano*, 2021, **15**, 15218–15228.

42 B. Guo, W. Du, T. Yang, J. Deng, D. Liu, Y. Qi, J. Jiang, S. J. Bao and M. Xu, *Adv. Sci.*, 2020, **7**, 1902617.

43 K. Liao, W. Ding, B. Zhao, Z. Li, F. Song, Y. Qin, T. Chen, J. Wan, M. Han and G. Wang, *Carbon*, 2011, **49**, 2862–2868.

44 H. Liu, J. Wang, C. Wang and Y. Xia, *Adv. Energy Mater.*, 2011, **1**, 1101–1108.

45 S. Hussain, X. Yang, M. K. Aslam, A. Shaheen, M. S. Javed, N. Aslam, B. Aslam, G. Liu and G. Qiao, *Chem. Eng. J.*, 2020, **391**, 123595.

46 K. Xu, P. Chen, X. Li, Y. Tong, H. Ding, X. Wu, W. Chu, Z. Peng, C. Wu and Y. Xie, *J. Am. Chem. Soc.*, 2015, **137**, 4119–4125.

47 P. Chen, K. Xu, Z. Fang, Y. Tong, J. Wu, X. Lu, X. Peng, H. Ding, C. Wu and Y. Xie, *Angew. Chem.*, 2015, **127**, 14923–14927.

48 B. S. Yeo and A. T. Bell, *J. Am. Chem. Soc.*, 2011, **133**, 5587–5593.

49 S. Chen, J. Luo, N. Li, X. Han, J. Wang, Q. Deng, Z. Zeng and S. Deng, *Energy Storage Mater.*, 2020, **30**, 187–195.

50 M. Ding, S. Huang, Y. Wang, J. Hu, M. E. Pam, S. Fan, Y. Shi, Q. Ge and H. Y. Yang, *J. Mater. Chem. A*, 2019, **7**, 25078–25087.

51 R. Wang, K. Wang, S. Gao, M. Jiang, J. Han, M. Zhou, S. Cheng and K. Jiang, *Nanoscale*, 2018, **10**, 16730–16737.

52 X. Liang, C. Hart, Q. Pang, A. Garsuch, T. Weiss and L. F. Nazar, *Nat. Commun.*, 2015, **6**, 1–8.

53 P. Zuo, J. Hua, M. He, H. Zhang, Z. Qian, Y. Ma, C. Du, X. Cheng, Y. Gao and G. Yin, *J. Mater. Chem. A*, 2017, **5**, 10936–10945.

54 D. Wang, Q. Cao, L. Li, B. Jing, Z. Yang, X. Wang, T. Huang, L. Liang, P. Zeng and J. Li, *ACS Appl. Mater. Interfaces*, 2021, **13**, 16374–16383.

55 M. Zhao, H. Peng, Z. Zhang, B. Li, X. Chen, J. Xie, X. Chen, J. Wei, Q. Zhang and J. Huang, *Angew. Chem., Int. Ed.*, 2019, **58**, 3779–3783.

56 H. Shao, W. Wang, H. Zhang, A. Wang, X. Chen and Y. Huang, *J. Power Sources*, 2018, **378**, 537–545.

57 W. Wang, Y. Zhao, Y. Zhang, J. Wang, G. Cui, M. Li, Z. Bakenov and X. Wang, *ACS Appl. Mater. Interfaces*, 2020, **12**, 12763–12773.

58 D. Luo, Z. Zhang, G. Li, S. Cheng, S. Li, J. Li, R. Gao, M. Li, S. Sy, Y. Deng, Y. Jiang, Y. Zhu, H. Dou, Y. Hu, A. Yu and Z. Chen, *ACS Nano*, 2020, **14**, 4849–4860.

59 S. Hussain, X. Yang, M. K. Aslam, A. Shaheen, M. S. Javed, N. Aslam, B. Aslam, G. Liu and G. Qiao, *Chem. Eng. J.*, 2020, **391**, 123595.